

# **Title:** Surface phase transitions and crystal growth rates of ice in the atmosphere

**Short Title:** Explaining the shape of snow crystals

**Authors:** Pablo Llombart,<sup>1,2</sup> Eva G. Noya,<sup>1</sup> and Luis G. MacDowell<sup>2\*</sup>

**Affiliations:** <sup>1</sup> Instituto de Química Física Rocasolano, Spain.

<sup>2</sup>Departamento de Química Física, Universidad Complutense de Madrid, Spain.

\*Correspondence to: lgmac@quim.ucm.es

**Abstract:** With climate modeling predicting a raise of at least 2 °C by year 2100, the fate of ice has become a serious concern, but we still do not understand how ice grows (or melts). In the atmosphere, crystal growth rates of basal and prismatic facets exhibit an enigmatic temperature dependence, and crossover up to three times in a range between 0 and -40°. Here we use large scale computer simulations to characterize the ice surface and identify a sequence of novel phase transitions on the main facets of ice crystallites. Unexpectedly, we find that as temperature is increased, the crystal surface transforms from a disordered phase with proliferation of steps, to a smooth phase with small step density. This causes the anomalous increase of step free energies and provides the long sought explanation for the enigmatic crossover of snow crystal growth rates found in the atmosphere.

**One Sentence Summary:** Atomic scale description of the ice structure predicts ice crystal growth rates and explains snow crystal shapes.

**Note:** A revised version with title "Surface phase transitions and crystal growth habits of ice in the atmosphere" accepted the 6th march 2020 to appear in Science Advances (in press).

**Main Text:**

## **Introduction**

The Nakaya diagram documents the hidden mystery of snow crystal growth [1, 2]: as temperature is cooled down from 0 to  $-40^{\circ}\text{C}$ , ice crystals in the atmosphere change their habit from plates, to columns, to plates and back to columns in a puzzling and unexplained sequence that holds the key to our understanding of the ice surface (Fig. 1).

After heterogeneous nucleation [3, 4], there still is a long way before ice crystallites adopt the micron size found in cirrus clouds [5]. Whether the ice embryos transform into mature columnar or plate like hexagonal prisms depends on the relative growth rate of basal and prismatic facets [6, 7]. But what drives the crossover of basal and prismatic growth rates, and how such changes are related to the ice surface structure remains completely unknown to date [8]. Kuroda and Lacmann speculated that the occurrence of surface phase transitions could result in sudden changes of the crystal growth rate, and provide an explanation for the observed crystal habits [9], but unfortunately the experimental verification of this hypothesis has remained elusive to date [10, 11, 12, 13] and our current understanding is still far from providing a molecular explanation [14, 15, 16, 13]. However, recent findings point to the significance of the heterogeneous in plane structure of ice's premelting film [17].

Here we show that, similar to under-cooled bulk water, the facets of ice exhibit a different phases as temperature is cooled down below  $0^{\circ}\text{C}$ . Particularly, we identify a transition from an Ordered Flat to a Disordered Flat Phase that is akin to microphase separation of terraces on the crystal surface [18, 19]. Upon increasing temperature, the premelting film thickness grows and the surface structure flattens again, resulting in the unexpected increase of nucleation step free energies and the crossover of crystal growth rates exactly as found in laboratory and atmospheric field studies [16, 20].

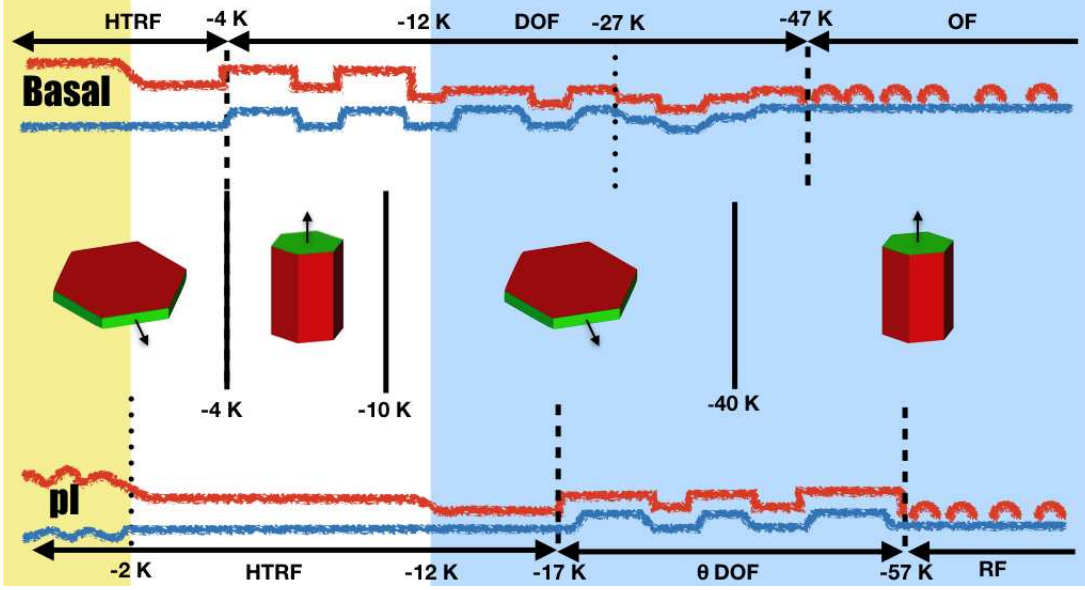


Figure 1: **Growth of ice crystals at low supersaturation.** Middle panel: As temperature  $\Delta T = T - T_t$  decreases below the triple point,  $T_t$ , the habit of hexagonal ice prisms grown in the atmosphere change sharply from plate like to columnar at ca. -4 K, from columnar to plate like at -10 K and somewhat less sharply from plate-like to columnar at -40 K [20]. The facet which grows faster as indicated by the arrows, dictates the prevalence of plates or columns. The change of crystal habits result from a crossover in the growth rates of the basal (red) and prismatic (green) facets. Top and bottom: Sketch of surface structural evolution with temperature as found in our work. Blue lines represent the i/f surface, and red lines represent the f/v surface. The basal surface (top row) is a High Temperature Reconstructed Flat phase from  $\Delta T = 0$  to -4 K. It becomes a Disordered Flat Phase in the range between ca. -4 K to -47 K and is transformed into an Ordered Flat phase at lower temperatures. In this phase, surface disorder resulting from patches of liquid-like molecules remains. The prismatic surface (bottom row) is a High Temperature Reconstructed Flat phase all the way from 0 K to -17 K, but is very close to the roughening transition at  $\Delta T > -2$  K in our model. In the range from -17 K to -57 K it is a Disordered Flat Phase and becomes an Ordered Flat phase below -57 K. At the transition from DOF like to HT-RF phases, step free energies increase anomalously and result in the crossover of crystal growth rates. The shaded areas illustrate the temperature range where melting of full bilayers has been accomplished. Blue, less than one full bilayer; white, less than two full bilayers; yellow, more than two full bilayers.

## Results

We perform large scale computer simulations of the TIP4P/Ice point charge model of water [21] on elongated rectangular surfaces meant to characterize large wave-length correlations along one direction. A bulk ice sample is placed in vacuum at temperatures below the model's triple point,  $T_t = 272$  K. After a few nanoseconds, the surface spontaneously develops a layer of quasi-liquid disordered molecules that can be readily distinguished from the underlying bulk crystal network (Fig.2-b). Averaging the position of the outermost solid and liquid-like atoms of the premelting layer about points  $\mathbf{r}$  on the plane of the interface, we are able to identify distinct ice/film,  $z_{if}(\mathbf{r})$  and film/vapor  $z_{fv}(\mathbf{r})$  surfaces [22], which separate the premelting film from the bulk solid and vapor, respectively (see Methods and Fig. S1) The average thickness of this layer grows from about 3 Å at  $\Delta T = T - T_t = -82$  K to 9 Å at  $\Delta T = -2$  K with little measurable anisotropy (Fig. S2) [23]. However, as recently observed for the basal plane in the mW model [17], this thin disordered layer is laterally inhomogeneous up to about  $\Delta T = -9$  K (Fig. 2-b and S3). Our study reveals that the heterogeneity is also found to a similar extent on the prismatic plane, with little qualitative differences (Fig. 3-b and Fig.S4). We quantify the  $\alpha = \{if, fv\}$  surface fluctuations along the long direction,  $x$ , by studying deviations of the local surface position,  $\delta z_\alpha(x)$ , about the average surface,  $\delta z_\alpha(x) = z_\alpha(x) - \bar{z}_\alpha$  (methods). This analysis is essential to reveal differences between basal and prismatic planes and allows us to identify a number of phase transitions along the sublimation line which cannot possibly be inferred from visual inspection of the snapshots (Fig 2-a, 3-a and Fig.S5, Fig.S6).

### Structure of the basal facet

At low temperature ( $\Delta T = -82$  K), the basal plane consists of a relatively ordered flat solid surface (OF), as revealed by a singly peaked, close to Gaussian distribution of both i/f and f/v surface fluctuations (Fig.2-a and Fig.S5-a). From the snapshots (Fig.2-b), the solid surface

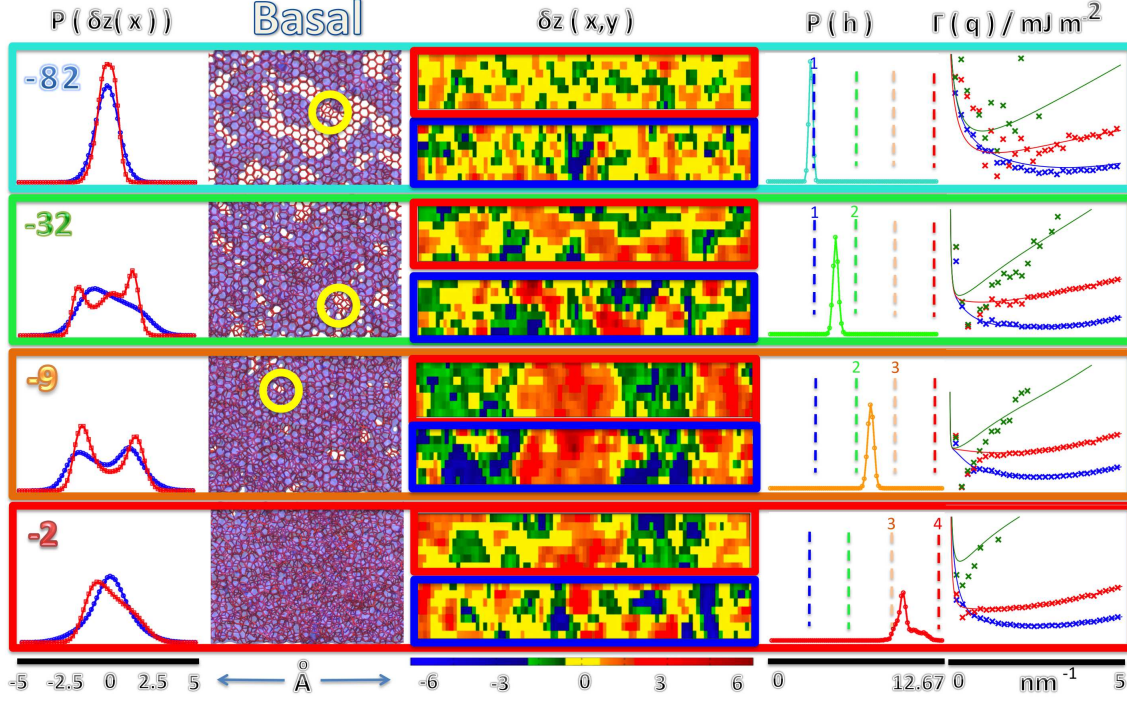


Figure 2: **Surface fluctuations on the basal facet.** a) Probability distribution of i/f (blue) and f/v (red) surface fluctuations, as measured by the deviations of the interface position  $z_\alpha(x)$  about the average surface  $\bar{z}_\alpha$ , for  $\alpha = \{if, fv\}$ . Results are shown for different temperatures as indicated in the legend. b) Snapshots of the basal surface at the same four temperatures. Red lines show the connected hydrogen bond network of all solid-like and liquid-like water molecules. The violet patches represent disordered liquid-like molecules. At low temperature the surface is mainly a regular hexagonal honeycomb, with a few patches of liquid-like molecules siting on interstitial positions (as indicated by the yellow circles). The extent of filled interstitial positions increases as the premelting layer extends on the surface. c) Plot showing a snapshot of local surface height fluctuations  $\delta z_{if}(\mathbf{r})$  (bottom, blue frame) and  $\delta z_{fv}(\mathbf{r})$  (top, red frame) on the basal ice face. Notice the emergence of large scale correlated patches for the DOF phase in the temperature range  $\Delta T = -32$  to  $-9$  K (See movie M1 and M2) The patches disappear at high temperature as the surface flattens again. d) Distribution of average film thickness,  $h$ , as temperature increases. Dashed vertical lines represent full layers in units of the molecular diameter. e) Wave-vector dependent stiffness coefficients, as obtained from the inverse surface structure factor for i/f correlations (blue), f/v correlations (red) and crossed i/f-f/v correlations (green). Crosses are results from simulation, full lines are fit to the SG+CW model. The results show that all surfaces are smooth, as indicated by the  $q \rightarrow 0$  divergence of  $\Gamma(q_x)$ . Notice the sharp minimum appearing at intermediate length scales in the temperature range  $\Delta T = -32$  K to  $-9$  K where the DOF phase is present.

is formed mainly of an oxygen-unreconstructed stack of chair hexagons [24, 25, 26]. Patches of disordered liquid-like molecules are found, and often show a tendency to sit on interstitial positions at the center of the primary hexagonal mesh (as in the so called Honeycomb Fletcher phase) [24]. The distribution remains uni-modal up to  $\Delta T = -52$  K, but somewhat broadens, revealing a large increase of disorder in this temperature interval which is consistent with observations of Sum Frequency Generation Spectroscopy [10]. At  $\Delta T = -42$  K, however, the distribution of  $\delta z_{fv}(x)$  develops a distinct trimodal character (Fig. S5-a). A main peak is centered at the mean surface position, and two other peaks appear to the left and right. The central peak of the trimodal distribution for  $\delta z_{fv}(x)$  gradually fades away into a bimodal, which persists up to  $\Delta T = -6$  K. In a narrow range between -9 K to -6 K, the distributions of  $\delta z_{fv}(x)$  and  $\delta z_{if}(x)$  are both fully bimodal and congruent. Finally, at the temperature of -2 K, the bimodal collapses sharply into one single uni-modal distribution.

From our analysis, the outer f/v surface of the premelting film exhibits a bimodal distribution centered at the mean surface location all the way from -22 K to -6 K. The onset of bimodality very much correlates with the vanishing of the (ppp-polarized) dangling OH bond stretch observed in SFG experiments [10]. The separation between peaks in the bimodal is approximately 3.1 Å, somewhat smaller than the expected bilayer distance of  $c/2 = 3.65$  Å. Furthermore, the bimodal evolves after the appearance at low temperature of a trimodal distribution with a main peak centered at the mean surface position, as if ice melting resulted in the formation of water-like molecules at half integer lattice positions (Extended Data Fig.S5-a).

## Preroughening and smoothening transitions

A strongly disordered phase consisting of a smooth surface with large scale step proliferation has been documented in the literature for Solid on Solid models (SOS) and is known as a disordered flat phase (DOF) [19]. Exactly as suggested by the extended SOS model, we observe

that the low temperature smooth flat phase transforms into a locally rough interface at a preroughening transition,  $\Delta T_{pr} \approx -47$  K [19]. However, contrary to the usual scenario, at high temperature the DOF phase does not undergo roughening, but rather, transforms across an apparently first order surface phase transition into a new flat phase at a *smoothing temperature*,  $\Delta T_s \approx -4$  K. This transition has not been previously reported but is consistent with existing surface phase diagrams for the extended SOS model [27, 28, 29]. Following the notation of SOS literature, we call this a High Temperature Reconstructed Flat phase (HT-RF).

As expected for the preroughening scenario, the transition to a DOF phase is strongly correlated with the growth of a premelting film in a loosely layer wise fashion [28, 18]. Clearly, we observe that the stabilization of the bimodal DOF phase at  $\Delta T = -22$  K results after the full formation of a second layer of premelted ice, as revealed by the mean location of premelting layer fluctuations in Fig.2-d (Fig. S5-b). The transition from DOF into the HT-RF phase is also accompanied by the formation of a full third premelted layer, as revealed by the shift in the premelting layer thickness from  $\Delta T = -9$  to  $-2$  K (Fig.2-d).

The DOF phase is not only characterized by step proliferation and strong local disorder. Also, the steps are highly correlated, and depending on the nature of the DOF phase, can exhibit diverging (finite) parallel correlations at a second (first) order preroughening transition [29]. We explore the extent of parallel correlations with a plot of the local surface height  $\delta z_{if}(\mathbf{r})$  and  $\delta z_{fv}(\mathbf{r})$  fluctuations (Fig.2-c), Fig. S7-a). At low temperature, the i/f surface exhibits small amplitude up and down domains, with small correlation lengths. At  $\Delta T = -9$  K, where the DOF phase is fully formed, we observe very large up and down domains of about 9 nm in length, that remain correlated over the full simulation box, as is visible both in the figure and in the accompanying movie ((M1 and M2). Our results are consistent with glancing angle x-ray experiments which reported the appearance of a large surface correlation length in the nanometer range, and the sharp disappearance of the long range correlations close to the triple

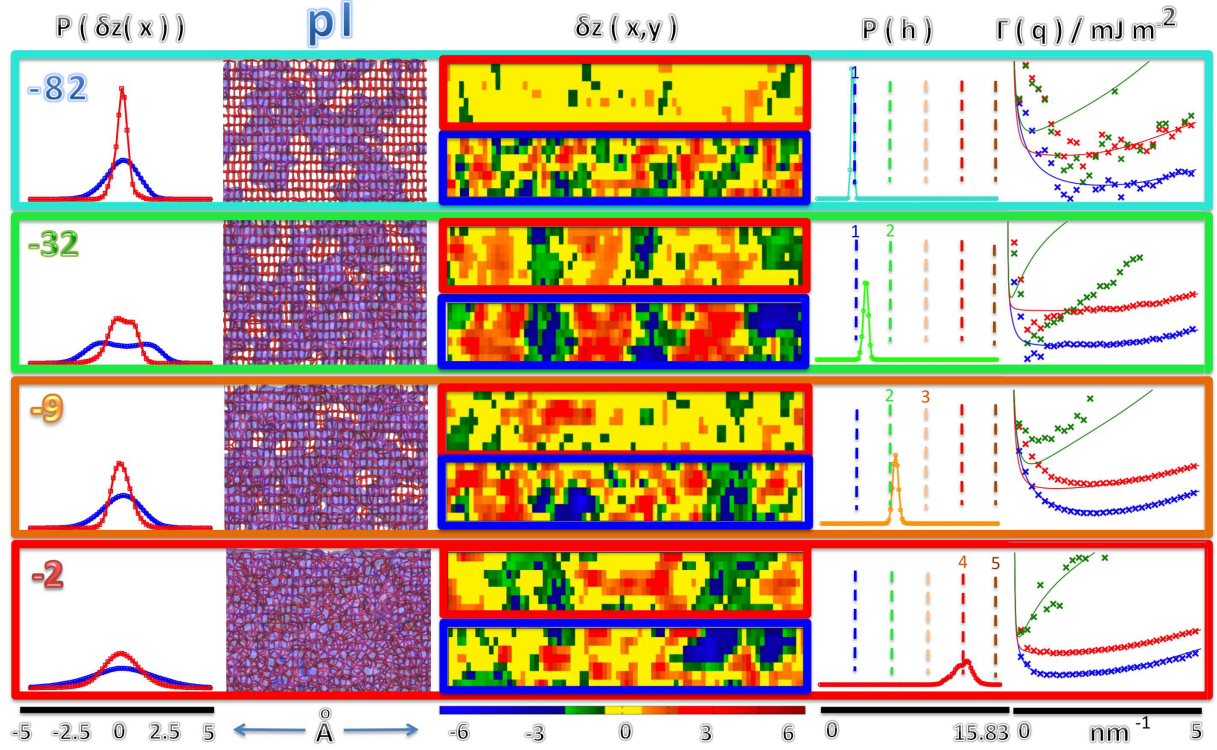


Figure 3: **Surface fluctuations on the prismatic facet.** Content displayed as in Fig.2. a) A bimodal distribution in this facet is only visible at temperature  $\Delta T = -32$  K. b) Here the snapshots show the characteristic rectangular mesh of the prismatic facet. At low temperature the liquid-like molecules form patches on the solid surface as in the basal face. c) Emergence of large correlated domains signal a DOF phase that is clearly visible at  $\Delta T = -32$  K and vanishes at significantly lower temperatures than for the basal facet (see movies M4 and M5 in Supplementary Materials Section) d) Notice the transition of premelting layer thickness across integer multiples of the molecular diameter occurs for the prismatic facet at the same temperature as for the basal facet. e) Likewise, the sharp minimum of the stiffness coefficient is visible only at and below  $\Delta T = -32$  K.

point [30].

The nature of these correlations can be quantified from the wave-vector dependent surface structure factor. Plots of the related effective stiffness,  $\Gamma_{\alpha\beta}(q_x) = \frac{k_B T}{A \langle z_\alpha(q_x) z_\beta(q_x) \rangle}$  are shown in Fig.2-e (Fig. S5-c). The results confirm that both at the prroughening and at the smoothening transition, the parallel correlations remain finite at  $q_x \rightarrow 0$ , as can be inferred from the strong divergence of the effective stiffness coefficients. Everywhere in the region where a DOF phase is present, however, the strongly correlated up and down domains are detectable as a sharp and deep minimum of the stiffness coefficients. A full theoretical description of this strong enhancement of large but finite correlations seems difficult. , which we attribute to non-Gaussian fluctuations of the correlated step heights. However, we can definitively observe in our results how the location of the sharp minima at intermediate wave-vectors decreases as the size of the correlated domains in Fig.2-c increase

## Structure of the Prismatic Facet

The study of surface fluctuations on the prismatic facet is significantly different. A low temperature flat phase, which preserves the expected low temperature rectangular mesh is observed at  $\Delta T = -82$  K (Fig.3-a and b). At this temperature, the distribution of both  $z_{if}(x)$  and  $z_{fv}(x)$  are unimodal but become gradually broader and skewed to the left as temperature is increased. At  $\Delta T = -32$  K, however, the distribution of  $z_{if}(x)$  and  $z_{fv}(x)$  become slightly bimodal. From  $\Delta T = -12$  K to  $\Delta T = -2$  K, the distribution becomes again completely unimodal and Gaussian like, but has broadened abruptly at  $\Delta T = -2$  K, signaling the approach of a roughening transition [31]. Although the order parameter is not sharp enough to reveal a strong bimodality, there appear a large number of steps in the range between -62 K to -22 K with distributions that seem to resemble a  $\theta$ DOF phase (similar to the DOF phase, but with a continuous change of the step coverage [28].) The transition from a DOF phase to a new high temperature reconstructed

flat phase (HT-RF) is visible in the surface maps (Fig 3-c), where large scale domains appear to end at -32 K. This is also visible in the surface structure factors depicted in Fig.3-e, which reveal again diverging stiffness coefficients at  $q_x \rightarrow 0$  (whence, flat phase), and the complete disappearance of the sharp minimum beyond this temperature (whence, loss of long range surface order). The transformation of the surface structure across the  $\theta$ DOF phase is also accompanied with continuous increase of the premelting film (Fig.3-d), but the transition from two to three layers and beyond appear to occur almost at the same temperature as in the basal facet. On the contrary, the transition from the  $\theta$ DOF phase to the HT-RF phases is distinctly different at the basal (ca.  $T_s = -4$  K) and the prismatic (ca.  $T_s = -27$  K) facets. Interestingly, these two temperatures, together with the full completion of a second bilayer at  $T_l = -12$  K are in very close agreement with the crystal habit changes observed in the Nakaya diagram.

We find that on average, both for the basal and the prismatic facets,  $z_{fv}(\mathbf{r})$  follows broadly the corrugation imposed by the  $z_{if}(\mathbf{r})$ , and the fluctuations of premelted film thickness appear as a broad unimodal distribution with no sign of bimodality or diverging correlation lengths (Fig.2-d and Fig.3-d). Accordingly, there are apparently no layering transitions along the sublimation line in the temperature range studied, at least in the thermodynamic sense. The lack of large correlation lengths of bimodality is very clearly observed in the surface plots of local film thickness  $h(\mathbf{r}) = z_{fv}(\mathbf{r}) - z_{if}(\mathbf{r})$  (Fig.4-a and movies M3 and M6) and is consistent with SFG experiments and preliminary indications for the mW model (Fig.S7-c and S8-c) [12, 17].

## Step Free Energies

The significance of DOF phases has been well documented [19, 27, 18]. The step proliferation is akin to a strong reduction of the step free energy, and the sharp decrease of the threshold for linear growth [27]. It is therefore expected that, as temperature raises across the smoothening transition from a DOF to a HT-RF phase, the crystal growth rates will decrease anomalously.

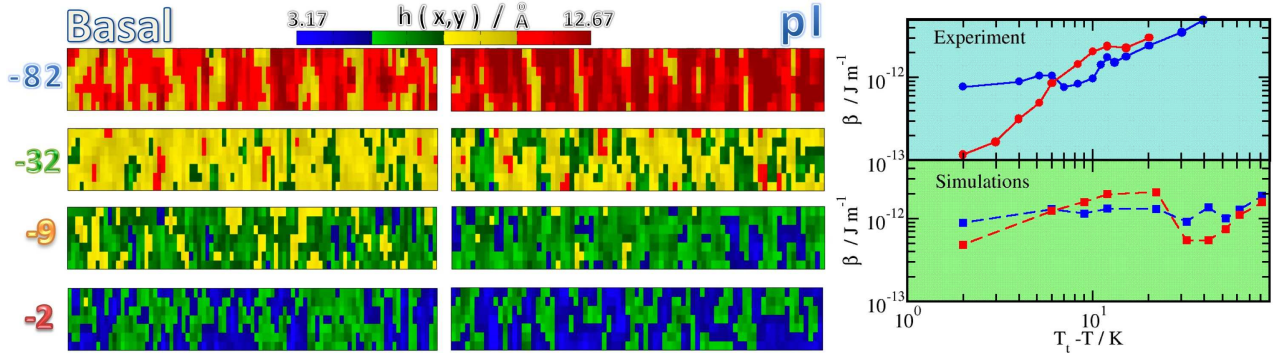


Figure 4: **Fluctuations of premelting thickness and step free energies** Figures a) and b) show a surface plot of instantaneous premelting thickness,  $h(\mathbf{r})$  for basal (a) and prismatic (b) surfaces (see movie M3 and M6 in Supplementary Materials section) Notice the absence of large correlated domains at all temperatures, in marked contrast with the  $\delta z_{if}(\mathbf{r})$  and  $\delta z_{fv}(\mathbf{r})$  surfaces shown in Fig.2 and Fig.3. c) Step free energies as obtained from a fit of the mean field SG+CW model to the regular (Gaussian) part of the stiffness coefficients in Fig.2-e,3-e for the basal (blue) and prismatic (red) facets. Results (squares with dashed lines) are compared to experimental data (circles with full lines) [16] and displayed on two different figures to avoid crowding. The step free energies from the fit exhibit a crossover at ca. -6 K, and overall a very similar trend as compared to experiment.

We provide a quantitative test of this expectation using a model of coupled capillary wave and sine Gordon Hamiltonians for the spectrum of surface fluctuations discussed recently (SG-CW) [22]. The capillary wave Hamiltonian describes the f/v surface fluctuations, while the likelihood of step proliferation in the underlying i/f surface is described with a sine Gordon Hamiltonian. Both models are coupled with an interface potential that sets the equilibrium film thickness as the difference between  $z_{fv}(\mathbf{r})$  and  $z_{if}(\mathbf{r})$ . The model can be fit to the regular (Gaussian) part of the surface stiffness, (Fig.2-e,3-e) and provides phenomenological coefficients for the surface tension and the step free energy,  $\beta$  (Methods). The non-monotonous behavior observed for  $\beta$  correlates with the behavior measured experimentally for terrace spreading rates [6], and is qualitatively very similar to step free energies obtained from growth measurements on snow crystals (Fig 4-b) [16]. Most importantly, our results confirm the suggested scenario of anomalous increase of  $\beta$  exactly at the smoothening transitions of basal and prismatic facets,

respectively.

## **Discussion**

Ice crystallites in the atmosphere are expected to grow by a two dimensional nucleation process. The crossover from column to plate like crystal habits that is observed experimentally can only proceed by a corresponding crossover in the relative growth rates of basal and prismatic facets. In our work, we show that in the range of about 80 K below the melting point, the main facets of ice may be found in up to three different surface phases with varying degree of surface disorder, as postulated by Kuroda and Lacmann with amazing intuition almost forty years ago [9]. The accompanying phase transitions provide the mechanism for a non-monotonous change of the relative step free energies for two dimensional nucleation. Most notably, we observe a premelting mediated process of surface smoothening, which results in the anomalous increase of step free energies. This results in the crossover of relative growth rates of basal and prismatic facets that is required to explain the Nakaya diagram.

The explanation of the long standing problem of snow crystal shapes (Fig.1) proofs that we have now a close to complete molecular description of the surface structure and crystal growth rates of ice in the atmosphere, with immediate implications for atmospheric sciences, glaciology and climate modeling.

## **Materials and Methods**

### **Force field**

Our study is performed with the TIP4P/Ice model of water [21]. This model was purposely designed to best describe the properties of ice. It predicts a melting point of  $T=272$  K, in excellent agreement with experiment, and reproduces the most relevant surface properties at this temper-

ature, such as liquid-vapor surface tension ( $\gamma_{lv} = 82$  mN/m calculated by ourselves, compared with  $\gamma_{lv} = 75.7$  mN/m from experiment), and solid-liquid surface tension ( $\gamma_{sl} = 29.8$  mN/m from Ref [32]. compared with recommended results  $\gamma_{sl} = 28$  mN/m by Pruppacher and Klett [33]). The precise location of the surface phase transitions observed here could somewhat change with the molecular model employed, but we expect the generic features to be quite generally observed for other accurate intermolecular potentials.

## Initial configurations

Initial configurations are prepared from a perfect unit cell in pseudo-orthorhombic arrangement, consisting of two layers of hexagonal rings perpendicular to the hexagonal  $c$  axis and a total of 16 water molecules. For the basal interface, we arrange a stack of  $46 \times 8 \times 8$  cells of 47,104 molecules, with the long direction,  $x$ , aligned along the  $b$  axis of the pseudo-orthorhombic cell, corresponding to the so called (basal)[pII] surface arrangement described by Davidchack and used in our previous work [34, 22, 35].

For the pI interface, the simulation box is prepared from a stack of  $40 \times 8 \times 8$  unit cells of  $N=40,960$  molecules, with the long direction,  $x$ , aligned along the  $a$  axis. This corresponds to the (basal)[pII] arrangement in our recent work. For each such arrangement, we prepare an independent hydrogen bond network as described in Ref. [36]. After forming the ice slab, we perform NpT simulations of the bulk solid at the desired temperature in order to obtain equilibrated unit cell dimensions. The solid is then scaled to the average equilibrium cell value, placed in vacuum, and equilibrated again in the NVT ensemble under periodic boundary conditions.

## Computation details

Large scale simulations are carried out on the Mare Nostrum IV facility at Barcelona Supercomputing center from the Spanish National Supercomputing Network. Classical Molecu-

lar Dynamics simulations are performed with the GROMACS package [37]. Trajectories are evolved with the velocity-verlet algorithm. Both the Lennard-Jones and Coulomb interactions are truncated at 0.9 nm. The electrostatic interactions are calculated using the Particle Mesh Ewald method. Simulations are thermostated with the velocity rescale algorithm [38], and the Berendsen barostat when required. A relaxation time of 2 ps is used for both the thermostat and barostat. The timestep employed is 0.003 ps. The simulations proceed over 0.9  $\mu$ s, with a long equilibration time of 225 ns and 675 ns for the production stage.

## Surface analysis

Prior to determining the i/f and f/v surfaces, we label water molecules as either solid or liquid-like, using the  $\bar{q}_6$  parameter [39]. Water like molecules are those with a  $\bar{q}_6$  parameter below a threshold  $\bar{q}_6^*(T)$ . In order to determine the threshold, we simulate the probability distribution of  $\bar{q}_6$  at a number of temperatures in either bulk solid or liquid water. The threshold value  $\bar{q}_6^*(T)$  is determined such that the number of mislabeled liquid molecules on the solid phase is equal to the number of mislabeled solid molecules on the liquid phase. A cluster analysis is performed to determine which molecules pertain to the condensed phase. Water molecules with oxygen atoms at a distance less than 3.5 Å belong to the same cluster. The i/f surface is determined from the positions of solid-like atoms in the largest solid cluster. We use the heights of the four topmost (or bottommost) solid atoms of the upper (lower) interface. At a given point  $\mathbf{r}$  on the plane of the interface, we find all the solid like atoms lying within a rectangular prism centered at  $\mathbf{r}$ . The base of the prism is taken to be that of the pseudo-orthorhombic unit cell of corresponding orientation. The surface height  $z_{\text{if}}(\mathbf{r})$  at that point is determined from the average location of the four uppermost solid like atoms. At the same point, the liquid surface for the upper (lower) interface is determined by averaging the position of the uppermost (bottom-most) for liquid-like molecules of the cluster of condensed molecules lying within a rectangular area

of  $3\sigma \times 3\sigma$  Lennard-Jones molecular diameters. The surfaces  $z_{\text{if}}(\mathbf{r})$  and  $z_{\text{fv}}(\mathbf{r})$  are determined over points on a grid on the plane of the interface. The grid has twice as many points as unit cells along the  $x$  direction, and just as many points as unit cells along the  $y$  direction. We perform the surface analysis from the set  $\{z_{\text{if}}(\mathbf{r})\}$  and  $\{z_{\text{fv}}(\mathbf{r})\}$  of points on the grid [22]. The instantaneous mean position of the i/f surface,  $\bar{z}_{\text{if}}$  is determined as the lateral average of  $\{z_{\text{if}}(\mathbf{r})\}$  over all points on the grid. From this value, we obtain  $\delta z_{\text{if}}(\mathbf{r}) = z_{\text{if}}(\mathbf{r}) - \bar{z}_{\text{if}}$ . The laterally averaged fluctuations  $\delta z_{\text{if}}(x)$  are obtained from  $\delta z_{\text{if}}(\mathbf{r})$  upon averaging along points  $y$ .  $\delta z_{\text{fv}}(\mathbf{r})$  and  $\delta z_{\text{fv}}(x)$  are obtained likewise. Fourier transforms of  $\delta z_{\text{if}}(x)$  and  $\delta z_{\text{fv}}(x)$  are obtained by summing  $\delta z_{\alpha}(x)e^{-iq_x x}$  over all points along  $x$ . Instantaneous local film heights are obtained as  $h(\mathbf{r}) = z_{\text{if}}(\mathbf{r}) - z_{\text{fv}}(\mathbf{r})$ . The instantaneous average film thickness is obtained from the mean of  $h(\mathbf{r})$  over the points of the grid.

## SG-CW model and fit

We describe the coupled i/f and f/v surface fluctuations with an extended Sine Gordon model for the i/f surface and the Capillary Wave model for the f/v surface [31]. The two terms are coupled via the interface potential,  $g(h)$ , with the premelting film thickness given by  $h(\mathbf{r}) = z_{\text{fv}}(\mathbf{r}) - z_{\text{if}}(\mathbf{r})$ . The full Hamiltonian is given by:

$$H = \int d\mathbf{r} \left[ \frac{\tilde{\gamma}_{iw}}{2} (\nabla z_{\text{if}})^2 + \frac{\gamma_{wv}}{2} (\nabla z_{\text{fv}})^2 + \gamma_{iv} \nabla z_{\text{if}} \cdot \nabla z_{\text{fv}} - u \cos(q_z z_{\text{if}}) + g(z_{\text{fv}} - z_{\text{if}}) \right] \quad (1)$$

where  $\tilde{\gamma}_{iw}$  is the bare stiffness coefficient,  $\gamma_{wv}$  is the water-vapor surface tension,  $\gamma_{iv}$  dictates the coupling of surface deformations,  $u$  accounts for the cost of moving the surface  $z_{\text{if}}$  away from integer lattice spacing,  $g(h)$  is the interface potential dictating the equilibrium film thickness, and  $q_z$  is the wave-vector for a wave-length equal to the lattice spacing. This Hamiltonian can be expanded to quadratic order in deviations away from the mean surface positions  $\bar{z}_{\text{if}}$  and  $\bar{z}_{\text{fv}}$ ,

and yields for the thermally averaged surface fluctuations [22]:

$$\begin{aligned}
\langle |z_{\text{if}}^2(\mathbf{q})| \rangle &= \frac{k_B T}{A} \frac{g'' + \gamma_{wv} q^2}{[v + g'' + \tilde{\gamma}_{iw} q^2][g'' + \gamma_{wv} q^2] - [g'' + \Delta g'' - \gamma_{iv} q^2]^2} \\
\langle |z_{\text{fv}}^2(\mathbf{q})| \rangle &= \frac{k_B T}{A} \frac{v + g'' + \tilde{\gamma}_{iw} q^2}{[v + g'' + \tilde{\gamma}_{iw} q^2][g'' + \gamma_{wv} q^2] - [g'' + \Delta g'' - \gamma_{iv} q^2]^2} \\
\langle z_{\text{if}}(\mathbf{q}) z_{\text{fv}}^*(\mathbf{q}) \rangle &= \frac{k_B T}{A} \frac{g'' + \Delta g'' - \gamma_{iv} q^2}{[v + g'' + \tilde{\gamma}_{iw} q^2][g'' + \gamma_{wv} q^2] - [g'' + \Delta g'' - \gamma_{iv} q^2]^2}
\end{aligned} \tag{2}$$

where  $g''$  is the second derivative of the interface potential at the equilibrium film thickness,  $\Delta g''$  accounts for enhanced coupled compression-expansion of the film thickness, and  $v = q_z^2 u$ . In practice, in order to avoid under-determined fits to limited data, we set  $\Delta g''$  and  $\gamma_{iv}$  to zero. This model for the spectrum of surface fluctuations has small and large wave-vector regimes. At large wave-vectors, the spectrum of fluctuations depends only on the stiffness and surface tension coefficients,  $\tilde{\gamma}_{iw}$  and  $\gamma_{wv}$  respectively [35]. As in extended capillary wave Hamiltonians, these are modeled as even polynomials of  $q$  to order 4. Once  $\tilde{\gamma}_{iw}$  and  $\gamma_{wv}$  are known, we fit the remaining parameters  $g''$  and  $v$  to match simultaneously the low wave-vector regime of  $q^2 \langle z_{\text{if}}(q) z_{\text{if}}(q) \rangle$ ,  $q^2 \langle z_{\text{fv}}(q) z_{\text{fv}}(q) \rangle$  and  $q^2 \langle z_{\text{if}}(q) z_{\text{fv}}(q) \rangle$  as obtained from simulations. The model reproduces very accurately the stiffness coefficients at high temperature. In the region where the DOF phase appears, it does however not grasp the enhanced height fluctuations. However, quite generally, the correlation functions may be expressed as a spectral series. The mean field solution corresponds to the 'trivial' eigenmode which results for the quadratic expansion of Hamiltonian. Higher order solutions yield additional eigenmodes. For strictly periodical height profiles, the spectrum of eigenmodes has a band structure. For the quasi-long range observed in the DOF phase, we expect the spectrum will not have continuous bands, but rather a region of close eigenvalues that are separated from the mean field mode. Accordingly, the effect of the inhomogeneity appears as an additive correction to the mean field solution. This allows us to obtain meaningful fits to the regular part of the spectrum merely by neglecting the strong

enhancement at intermediate length scales. The step free energy for the uncoupled Sine Gordon model can be obtained from the parameters  $\tilde{\gamma}_{iw}$  and  $v$  as  $\beta_{iw} = (8/q_z^2)(\gamma_{iw}v)^{1/2}$  [40, 35]. Since we find that the premelting film thickness is unimodal, a step on the i/f surface will provoke a similar step on the f/v surface, with a step energy of  $\beta_{wv} = (8/q_z^2)(\gamma_{wv}g'')^{1/2}$ . The cost of creating a step on the premelting film is therefore the sum  $\beta = \beta_{iw} + \beta_{wv}$ , which we use as an estimate for the step free energy of the ice/vapor interface in Fig.4.

## References

- [1] Nakaya, U. *Snow Crystals: Natural and Artificial* (Harvard University Press, Cambridge, 1954).
- [2] van den Heuvel, A. P. & Mason, B. J. Habit of ice crystals grown in hydrogen, carbon dioxide and air at reduced pressure. *Nature* **184**, 519–520 (1959).
- [3] Kiselev, A. *et al.* Active sites in heterogeneous ice nucleation—the example of k-rich feldspars. *Science* (2016).
- [4] Qiu, Y. *et al.* Ice nucleation efficiency of hydroxylated organic surfaces is controlled by their structural fluctuations and mismatch to ice. *J. Am. Chem. Soc.* **139**, 3052–3064 (2017).
- [5] Peter, T. *et al.* When dry air is too humid. *Science* **314**, 1399–1402 (2006).
- [6] Sei, T. & Gonda, T. The growth mechanism and habit change of ice crystals growing from the vapor phase. *J. Cryst. Growth* **94**, 697–707 (1989).
- [7] Demange, G., Zapolsky, H., Patte, R. & Brunel, M. A phase field model for snow crystal growth in three dimensions. *npj Comp. Mat.* **3**, 15 (2017).

- [8] Furukawa, Y. & Wettlaufer, J. Snow and ice crystals. *Phys. Today* **60**, 70–71 (2007).
- [9] Kuroda, T. & Lacmann, R. Growth kinetics of ice from the vapour phase and its growth forms. *J. Cryst. Growth* **56**, 189–205 (1982).
- [10] Wei, X., Miranda, P. B. & Shen, Y. R. Surface vibrational spectroscopic study of surface melting of ice. *Phys. Rev. Lett.* **86**, 1554–1557 (2001).
- [11] Bluhm, H., Ogletree, D. F., Fadley, C. S., Hussain, Z. & Salmeron, M. The premelting of ice studied with photoelectron spectroscopy. *J. Phys.: Condens. Matter* **14**, L227–L233 (2002).
- [12] Smit, W. J. & Bakker, H. J. The surface of ice is like supercooled liquid water. *Angew. Chem. Int. Ed. Engl.* **56**, 15540–15544 (2017).
- [13] Slater, B. & Michaelides, A. Surface premelting of water on ice. *Nat. Rev. Chem* **3**, 172–188 (2019).
- [14] Bartels-Rausch, T. Ten things we need to know about ice and snow. *Nature* **494**, 27–29 (2013).
- [15] Ball, P. Material witness: Close to the edge. *Nature Mat.* **15**, 1060 (2016).
- [16] Libbrecht, K. G. Physical dynamics of ice crystal growth. *Annu.Rev.Mater.Res* **47**, 271–295 (2017).
- [17] Qiu, Y. & Molinero, V. Why is it so difficult to identify the onset of ice premelting? *J. Phys. Chem. Lett.* **9**, 5179–5182 (2018).
- [18] Jagla, E. A., Prestipino, S. & Tosatti, E. Surface-melting-induced preroughening. *Phys. Rev. Lett.* **83**, 2753–2756 (1999).

- [19] Rommelse, K. & den Nijs, M. Preroughening transitions in surfaces. *Phys. Rev. Lett.* **59**, 2578–2581 (1987).
- [20] Bailey, M. P. & Hallett, J. A comprehensive habit diagram for atmospheric ice crystals: Confirmation from the laboratory, aircraft, and other field studies. *J. Atmos. Sci.* **66**, 2888–2899 (2009).
- [21] Abascal, J. L. F., Sanz, E., Fernandez, R. G. & Vega, C. A potential model for the study of ices and amorphous water: Tip4p/ice. *J. Chem. Phys.* **122**, 234511 (2005).
- [22] Benet, J., Llombart, P., Sanz, E. & MacDowell, L. G. Premelting-induced smoothening of the ice-vapor interface. *Phys. Rev. Lett.* **117**, 096101 (2016).
- [23] Conde, M. M., Vega, C. & Patrykiewicz, A. The thickness of a liquid layer on the free surface of ice as obtained from computer simulation. *J. Chem. Phys.* **129**, 014702 (2008).
- [24] Fletcher, N. H. Reconstruction of ice crystals at low temperatures. *Phil. Mag. B* **66**, 109–115 (1992).
- [25] Buch, V., Groenzin, H., Li, I., Schultz, M. J. & Tosatti, E. Proton order in the ice crystal surface. *Proc. Nat. Acad. Sci.* **105**, 5969–5974 (2008).
- [26] Pan, D. *et al.* Surface energy and surface proton order of the ice Ih basal and prism surfaces. *J. Phys.: Condens. Matter* **22**, 074209 (2010).
- [27] Prestipino, S., Santoro, G. & Tosatti, E. Preroughening, diffusion, and growth of a fcc(111) surface. *Phys. Rev. Lett.* **75**, 4468–4471 (1995).
- [28] Weichman, P. B. & Prasad, A. Zippering and intermeshing: Novel phase diagrams for interfaces and films. *Phys. Rev. Lett.* **76**, 2322–2325 (1996).

- [29] Bastiaansen, P. J. M. & Knops, H. J. F. Roughening and preroughening in the six-vertex model with an extended range of interaction. *Phys. Rev. B* **53**, 126–135 (1996).
- [30] Dosch, H., Lied, A. & Bilgram, J. H. Glancing angle x-ray scattering studies of the premelting of ice surfaces. *Surf. Sci.* **327**, 145–164 (1995).
- [31] Weeks, J. D. The roughening transition. In T., R. (ed.) *Ordering in Strongly Fluctuating Condensed Matter Systems*, 293–317 (Plenum, New York, 1980).
- [32] Espinosa, J. R., Vega, C. & Sanz, E. Ice-water interfacial free energy for the tip4p, tip4p/2005, tip4p/ice, and mw models as obtained from the mold integration technique. *J. Phys. Chem. C* **120**, 8068–8075 (2016).
- [33] Pruppacher, H. R. & Klett, J. D. *Microphysics of Clouds and Precipitation* (Springer, Heidelberg, 2010).
- [34] Davidchack, R. L., Morris, J. R. & Laird, B. B. The anisotropic hard-sphere crystal-melt interfacial free energy from fluctuations. *J. Chem. Phys.* **125**, 094710 (2006).
- [35] Benet, J., Llombart, P., Sanz, E. & MacDowell, L. G. Structure and fluctuations of the premelted liquid film of ice at the triple point. *Mol. Phys.* 1–19 (2019).
- [36] Buch, V., Sandler, P. & Sadlej, J. Simulations of H<sub>2</sub>O solid, liquid and clusters, with an emphasis on ferroelectric ordering transition in hexagonal ice. *J. Phys. Chem. B* **102**, 8641–8653 (1998).
- [37] Hess, B., Kutzner, C., van der Spoel, D. & Lindahl, E. Gromacs 4: Algorithms for highly efficient, load-balanced, and scalable molecular simulation. *J. Chem. Theo. Comp.* **4**, 435–447 (2008).

- [38] Bussi, G., Donadio, D. & Parrinello, M. Canonical sampling through velocity rescaling. *J. Chem. Phys.* **126**, 014101 (2007).
- [39] Lechner, W. & Dellago, C. Accurate determination of crystal structures based on averaged local bond order parameters. *J. Chem. Phys.* **129**, 114707 (2008).
- [40] Nozières, P. & Gallet, F. The roughening transition of crystal surfaces. i. static and dynamic renormalization theory, crystal shape and facet growth. *J. Phys.(Paris)* **48**, 353–367 (1987).

## Acknowledgments

We thank E. Lomba for helpful discussions and J. L. F. Abascal for invaluable support.

## Funding

We acknowledge funds from the Spanish Agencia Estatal de Investigación under Grant No. FIS2017-89361-C3-2-P. This project was made possible thanks to the use of the Mare-Nostrum supercomputer and the technical support provided by Barcelona Supercomputing Center from the Spanish Network of Supercomputing (RES) under grants QCM-2017-2-0008 and QCM-2017-3-0034.

## Author Contributions

P.L. performed programs and simulations, analyzed the data and discussed results as part of his PhD Thesis. E.G.N. supervised and discussed results. L.G.M. conceived the project, interpreted results and wrote the paper.

## Competing interests

The authors declare no competing financial interests.

## Supplementary Figures S1 to S8

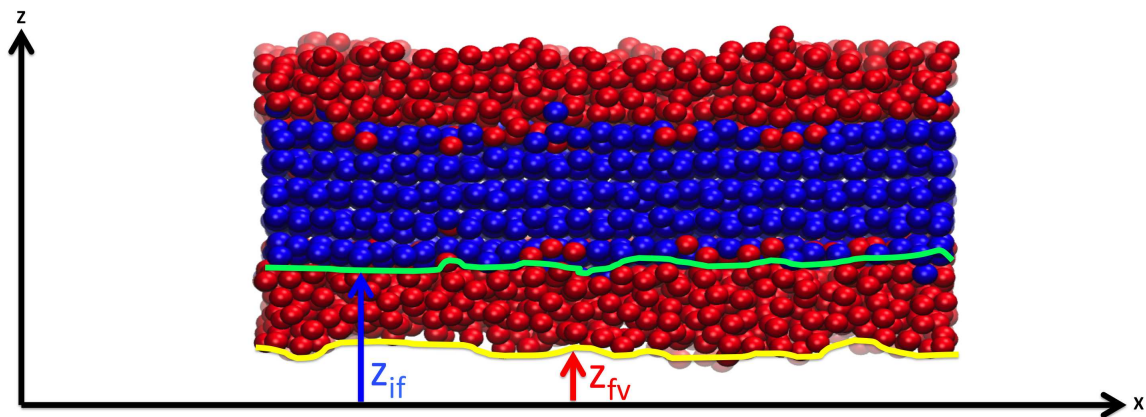


**Fig. S1: Characterization of the premelting layer.** Snapshot of a bulk ice slab in equilibrium with pure water vapor. After placing a slab of perfect ice in vacuum, a premelting layer of disordered water molecules is formed spontaneously in a few nanoseconds. Using a suitable order parameter it is possible to label liquid-like from solid-like molecules. The state of the premelting film may be described in terms of two different surfaces,  $z_{if}$  and  $z_{fv}$ , separating the film from bulk solid and vapor phases, respectively.

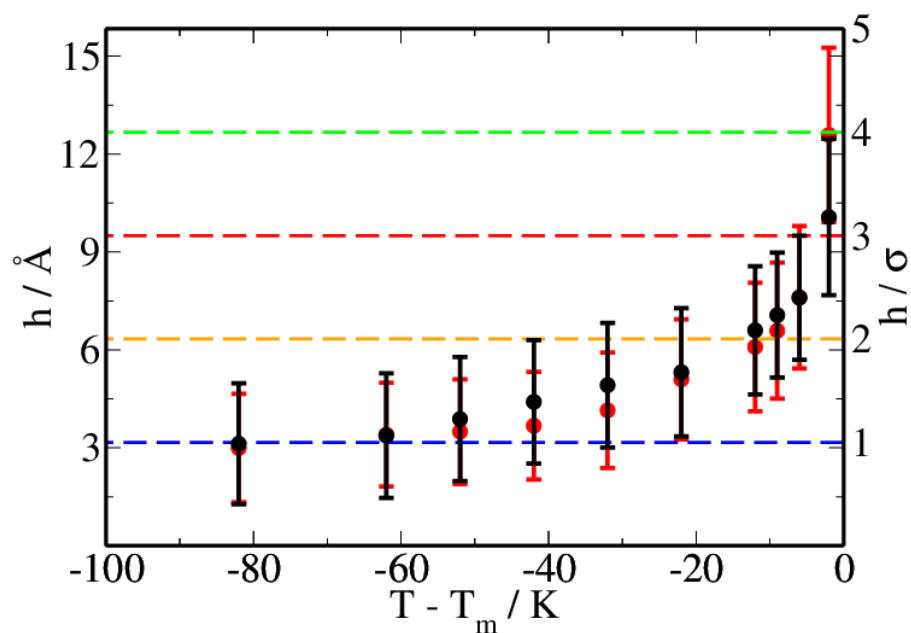


**Fig.S2: Premelting film thickness as a function of temperature for basal and prismatic faces.** Figure shows the thermally averaged film thickness  $h$  of the basal (black) and prismatic (red) planes. Dashed lines indicate multiples of the molecular diameter as measured in units of the Lennard-Jones  $\sigma$  parameter. The thickness of the prismatic plane remains only slightly below that of the basal plane up to 270 K, where the prismatic plane premelts by almost one full bilayer more

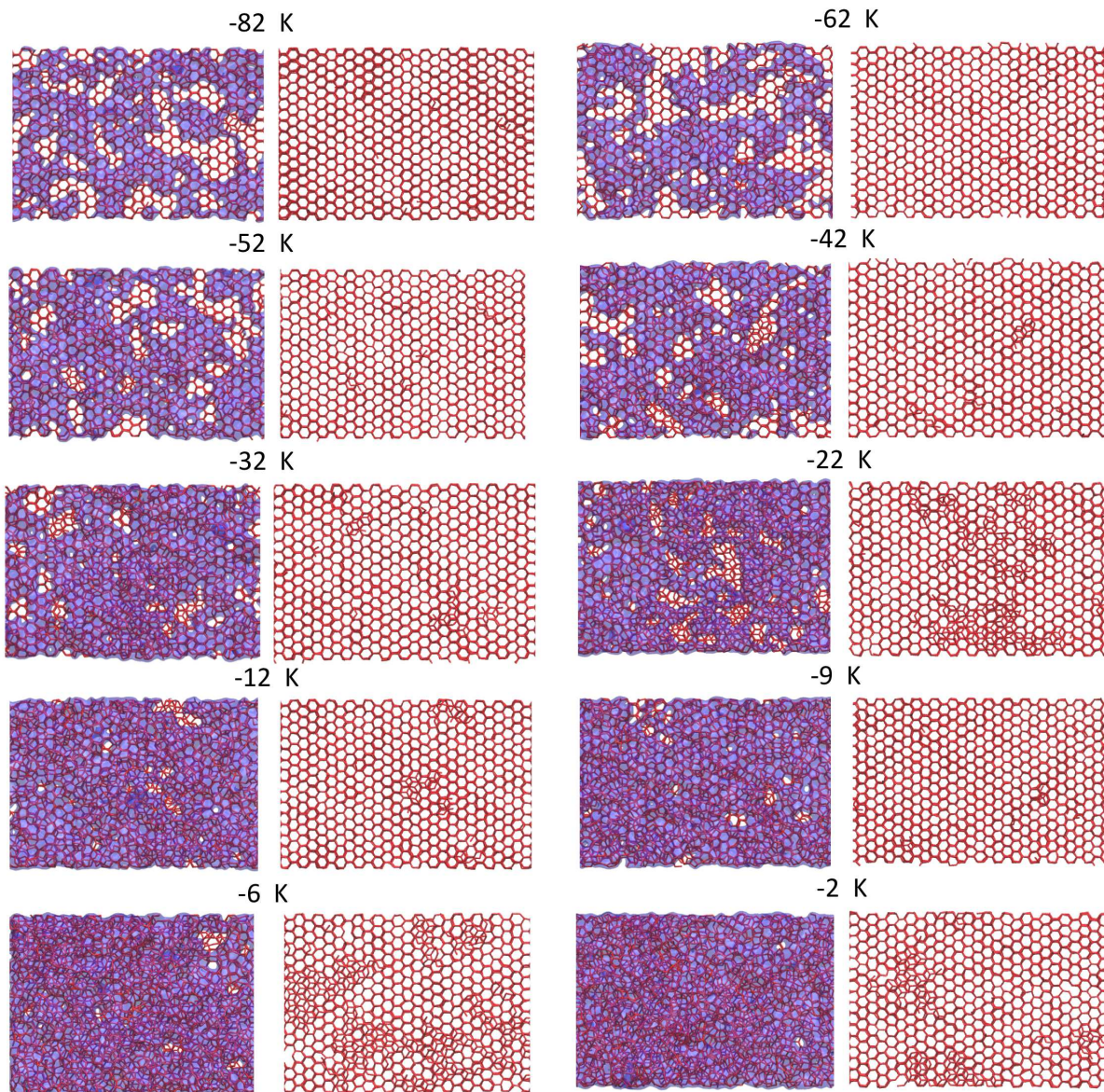


**Fig.S3: Evolution of surface structure with temperature on the basal face.** The first and third columns show the position of all atoms in the cluster of condensed molecules (solid-like or liquid-like), projected onto the x-y plane. The red wire-frame joins atoms separated by less than 3.5 Å, which is the same criteria used to define first neighbours in the algorithm to search for solid clusters. Liquid-like atoms are further coloured in violet. The typical hexagonal honeycomb is clearly visible on patches not covered by premelted water-like molecules. Also notice how the premelted molecules often occupy interstitial positions on the center of the hexagonal honeycomb. The second and third columns show only the positions of solid-like atoms, with liquid-like atoms left apart. As far as the position of oxygen atoms, the surface remains unreconstructed in all the temperature domain. Patches of stacking disordered ice appear at temperatures  $\Delta T = -22$  and  $-2$  K consistent with the melting of complete solid bilayers.

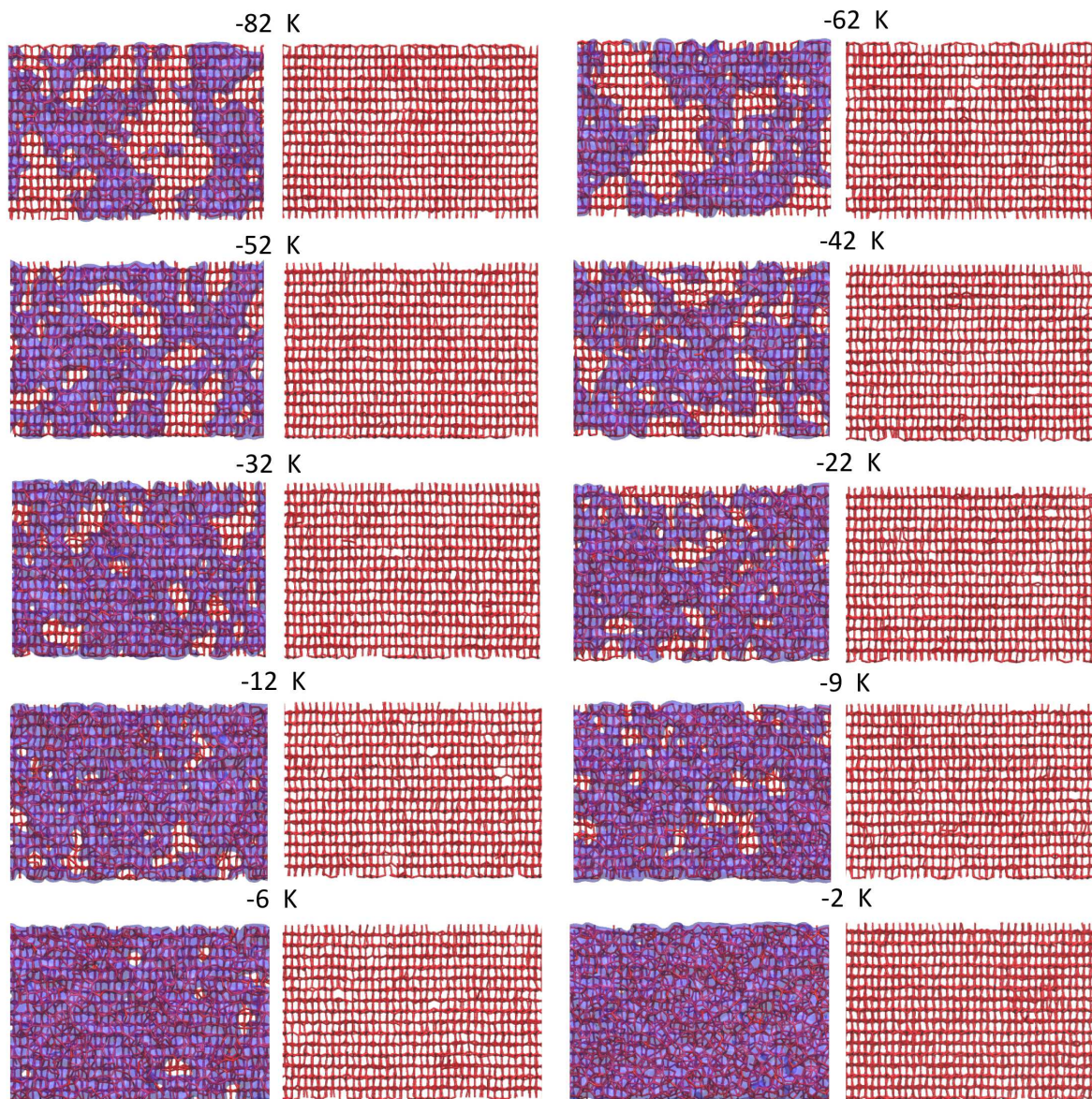


**Fig.S4: Evolution of surface structure with temperature on the prismatic face.** The first and third columns show the position of all atoms in the cluster of condensed molecules (solid-like or liquid-like) projected onto the x-y plane. The red wire-frame joins atoms separated by less than 3.5 Å, which is the same criteria used to define first neighbours in the algorithm to search for solid clusters. Liquid-like atoms are further coloured in violet. The typical rectangular structure of prismatic faces is clearly visible on patches not covered by premelted water-like molecules. The second and third columns show only the positions of solid-like atoms, with liquid-like atoms left apart. The oxygen framework remains unreconstructed in all the temperature domain.

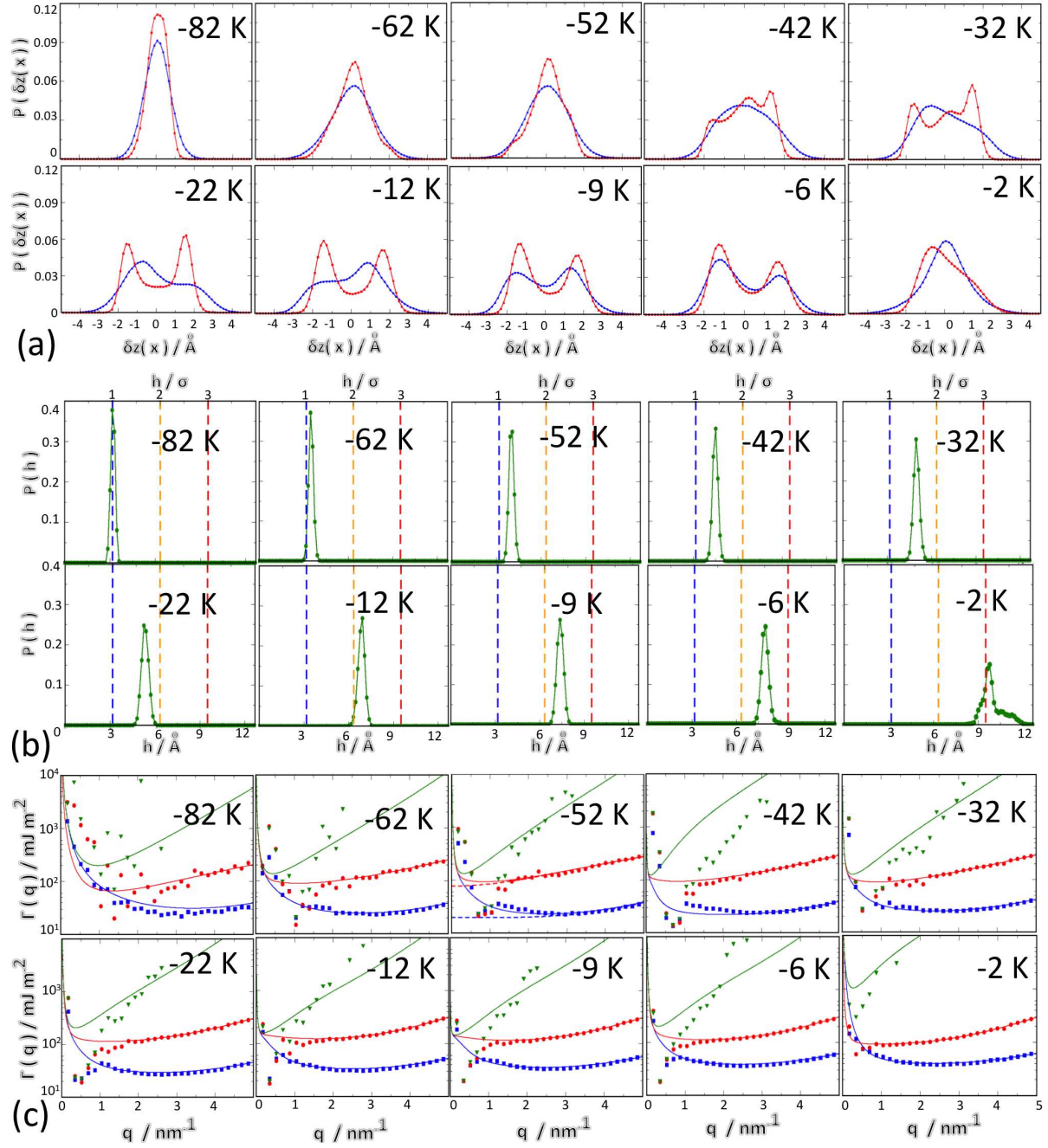


**Fig.S5: Surface fluctuations on the basal face at all studied temperatures.** a) Probability distribution of i/f (blue) and f/v (red) surface fluctuations, as measured by the deviations of the interface position along  $x$  about the average surface. b) Probability distribution of the global premelting layer thickness,  $h$ , on the basal face for several temperatures as indicated in the color code. The vertical dashed lines indicate the location of multiples of the layer thickness in units of the molecular diameter ( $\sigma$  parameter of the Lennard-Jones bead in the TIP4P/Ice model). c) Spectrum of fluctuations on the basal face. The figure shows wave-vector dependent stiffness coefficients, as obtained from the inverse surface structure factor for i/f correlations (blue), f/v correlations (red) and crossed i/f - f/v correlations (green). Symbols are results from simulations. The full lines are a fit to the small wave-vector results to the SG+CW model, using as input results from the large wave-vector fit shown in dashed lines.

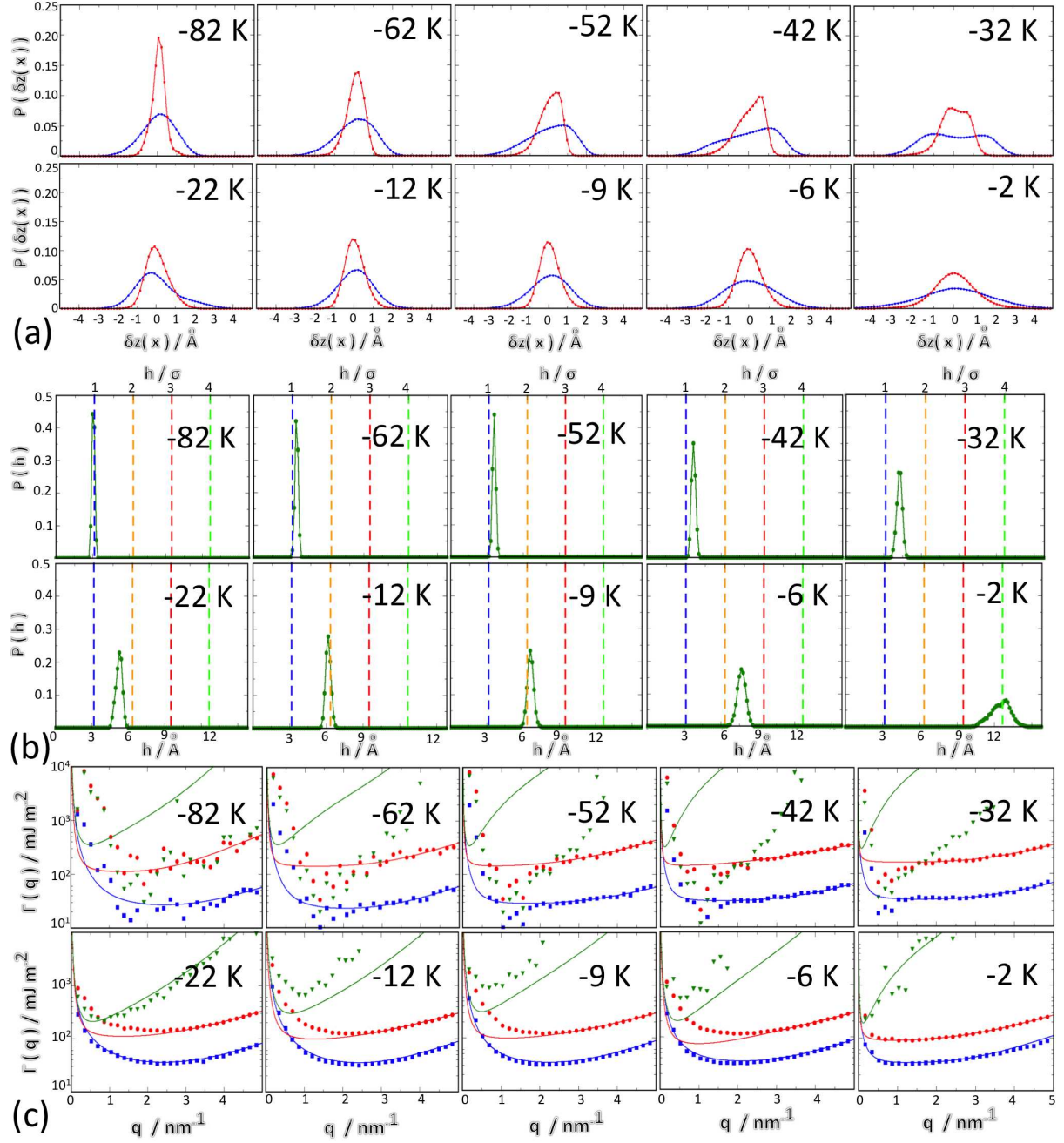


**Fig.S6: Surface fluctuations on the prismatic face at all studied temperatures.** a) Probability distribution of i/f (blue) and f/v (red) surface fluctuations, as measured by the deviations of the interface position along  $x$  about the average surface. b) Probability distribution of the local height fluctuations  $\delta z(\mathbf{r})$ . c) Probability distribution of the global premelting layer thickness,  $h$ , on the basal face for several temperatures as indicated in the color code. The vertical dashed lines indicate the location of multiples of the layer thickness in units of the molecular diameter ( $\sigma$  parameter of the Lennard-Jones bead in the TIP4P/Ice model). c) Spectrum of fluctuations on the basal face. The figure shows wave-vector dependent stiffness coefficients, as obtained from the inverse surface structure factor for i/f correlations (blue), f/v correlations (red) and crossed i/f-f/v correlations (green). Symbols are results from simulations. The full lines are a fit to the small wave-vector results to the SG+CW model, using as input results from the large wave-vector fit shown in dashed lines. 26

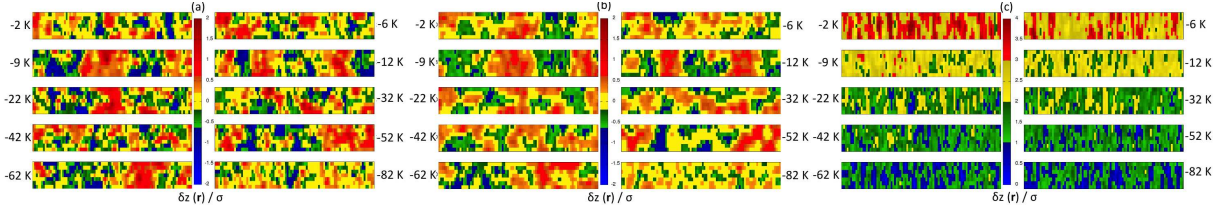


**Fig.S7: Surface plots of local height fluctuations for the basal face.** a) Local height fluctuations  $\delta z_{if}(\mathbf{r})$  of the i/f surface (see M1). b) Local height fluctuations  $\delta z_{fv}(\mathbf{r})$  of the f/v surface (see M2). At low and high temperatures, the correlation lengths are small and one finds alternated red and blue patches of small size. At intermediate temperatures there appear large red and blue patches indicative of the emergence of large correlations of preferred wave-length. In this regime, comparison of a) and b) shows that the i/f and f/v surfaces are also highly correlated. c) Local fluctuations of film thickness  $h(\mathbf{r})$  (see M3). The correlation length of  $\delta h(\mathbf{r})$  remains small at all temperatures as is visible from the small size of alternating patches. The thickening of the films as temperature increases is apparent from the change in color code.

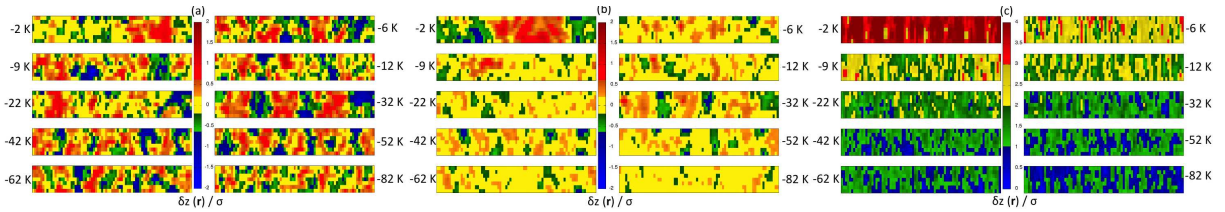


**Fig.S8: Surface plots of local height fluctuations for the prismatic face.** a) Local height fluctuations  $\delta z_{if}(\mathbf{r})$  of the i/f surface (see M4). At low temperatures the alternation of small blue and red domains is indicative of small correlation lengths. The size of the domains increases significantly at a DOF phase at  $T=240$  K and then decrease again. At the highest temperature,  $T=270$  K, a large correlated domain that spans most of the simulation cell is indicative of the approach to a roughening transition. b) Local height fluctuations  $\delta z_{fv}(\mathbf{r})$  of the f/v surface (see M5). The temperature evolution of correlation lengths is similar to that of the i/f , but compared to the basal surface, the amplitude of the fluctuations here is much smaller. c) Local fluctuations of film thickness  $h(\mathbf{r})$  (see M6). As for the basal face, the correlation length of  $\delta h(\mathbf{r})$  remains small at all temperatures as is visible from the small size of alternating patches. The thickening of the films as temperature increases is apparent from the change in color code.

## Supplementary Movies M1 to M6

- Movie M1: Local height fluctuations  $\delta z_{if}(\mathbf{r})$  of the i/f surface for the basal plane (see also Fig.S7).
- Movie M2: Local height fluctuations  $\delta z_{fv}(\mathbf{r})$  of the f/v surface for the basal plane (see also Fig.S7).
- Movie M3: Local fluctuations of film thickness  $h(\mathbf{r})$  for the basal plane (see also Fig.S7).
- Movie M4: Local height fluctuations  $\delta z_{if}(\mathbf{r})$  of the i/f surface for the prismatic plane (see also Fig.S8).
- Movie M5: Local height fluctuations  $\delta z_{fv}(\mathbf{r})$  of the f/v surface for the prismatic plane (see also Fig.S8)
- Movie M6: Local fluctuations of film thickness  $h(\mathbf{r})$  for the prismatic plane (see also Fig.S8).